



# Graphene-decorated magnetic cobalt ferrite for effective UV-accelerated photocatalytic degradation of methylene blue: experimental and theoretical insights by DFT

G. Nandhini<sup>1</sup> · D. Vignesh<sup>2</sup> · M. K. Shobana<sup>1</sup> · T. Pazhanivel<sup>3</sup> · S. Kavita<sup>4</sup> · P. Balaji<sup>3</sup>

Received: 19 February 2024 / Accepted: 13 July 2024  
© Qatar University and Springer Nature Switzerland AG 2024

## Abstract

Graphitic carbon-based nanocomposites have drawn considerable attention in nanoscience due to their intriguing property and biocompatible behavior. This study enumerates the structural, optical, and magnetically dependent applications of pure and graphene oxide (GO)-modified  $\text{CoFe}_2\text{O}_4$  spinel nanoferrites across diverse domains via experimental (sol-gel combustion) and theoretical insights (Density Functional Theory (DFT) simulations). The structural analysis suggests an inverse spinel structure with an average crystalline size of 27.78 and 40.25 nm for dual nanoferrites ( $\text{CoFe}_2\text{O}_4$  and  $\text{CoFe}_2\text{O}_4\cdot\text{GO}$ ), respectively. Further,  $\text{O}^{2-}$  coordination to binary interstices (tetrahedral and octahedral) increases the specific surface area (SSA) for active charge transfer and photocatalytic activity. The observed degradation result exhibits that the  $\text{CoFe}_2\text{O}_4\cdot\text{GO}$  nanocomposites show a higher efficiency of 87.74% compared with pure  $\text{CoFe}_2\text{O}_4$  nano ferrites (53.10%). In addition, the vibrating sample magnetometer shows good magnetic behavior for pure  $\text{CoFe}_2\text{O}_4$  nanoferrites than  $\text{CoFe}_2\text{O}_4$ /graphene oxide nanocomposites with the maximum saturation magnetization value of 63.74 and 56.60 emu/g, respectively. Hence, the results suggest that  $\text{CoFe}_2\text{O}_4\cdot\text{GO}$  nanocomposite is more highly suitable for wastewater treatment applications due to its higher efficiency rate of degradation.

**Keywords** Cobalt ferrite · Graphene oxide · Degradation · Magnetic behavior · Density function theory

## 1 Introduction

Wastewater from the paint industries and fabrics are particularly high in pollutants, particularly colors such as methyl orange, rhodamine B, methylene blue (MB), phenol, methyl, etc. These contaminants cause substantial health

consequences and may have an impact on both humans as well as aquatic organisms [1]. So, one of the main focuses of the experts has been the elimination of such pollutants. Since it transforms the aforementioned pollutants into innocuous compounds, photocatalytic oxidation is one of the more popular contemporary techniques. Ferrites can be utilized in pollution removal processes to significantly improve the process of recovering powdered adsorbent materials from solvents using externally generated magnetic fields [2, 3]. They are exceedingly durable and retain their qualities even after being manufactured and utilized repeatedly. Due to their distinctive qualities, such as strong pollutant adsorption capabilities and as an outstanding photocatalyst, ferrites are well known in several forms of wastewater management for pollutant removal by adsorption and photodegradation [4].

Many current photocatalysts, such as titanium dioxide ( $\text{TiO}_2$ ), suffer from limitations such as wide bandgaps that only utilize a small portion of the solar spectrum, thus limiting efficiency. Research is needed to develop new materials

✉ M. K. Shobana  
mkshobana@gmail.com

<sup>1</sup> Department of Physics, School of Advanced Sciences, Vellore Institute of Technology, Vellore, Tamil Nadu 632014, India

<sup>2</sup> Birla Institute of Technology, Mesra, Ranchi, Jharkhand 835215, India

<sup>3</sup> Smart Materials Interface Laboratory, Department of Physics, Periyar University, Salem, Tamil Nadu 636011, India

<sup>4</sup> Centre for Automotive Energy Materials, International Advanced Research Centre for Powder Metallurgy and New Materials (ARCI), IIT-M Research Park, Chennai, Tamil Nadu 600113, India

or modify existing ones to enhance light absorption across a broader spectrum, including visible light. Most photocatalysts degrade over time due to photo corrosion or other factors, reducing their effectiveness. To overcome this problem, carbon-based nanoferrite materials are extensively used in photocatalytic applications owing to their suitable band structure, good chemical stability, durability, sustained catalytic activity over extended periods of operation, simplifies catalyst retrieval and recycling, and electronic configuration that facilitates the separation of photo-excited electron-hole pairs. This separation prevents the recombination of charges, thereby enhancing the photocatalytic activity. Thus, graphene oxide-based nanoferrites are significantly employed for enhanced degradation activity.

According to the synthesis process and environmental factors, cobalt ferrite nanoparticles might fundamentally result in either an inverse or mixed kind of spinel ferrite. Despite having a constant chemical composition, the super-exchange interaction ( $\text{Fe}_A^{3+}\text{-Fe}_B^{3+}$ ) is different from the  $\text{Co}_A^{2+}\text{-Fe}_B^{3+}$  interaction, which causes changes in the cation allocation A (tetrahedral) and B (octahedral) sites in the spinel based on their bond length. The difference in site allocation (A and B sites) results in different magnetic properties [5]. Combining cobalt ferrite with strong electron conductors like graphene improves its photocatalytic activity. Due to its unique qualities, including high mechanical stiffness, superior charge-carrier mobility, high specific surface area (SSA), and high thermal conductivity for the creation of photocatalyst composites, graphene has attracted significant attention. Consequently, by employing graphene, it becomes possible to develop photocatalysts that exhibit greater photocatalytic activity [6]. The sol-gel combustion process is another commonly used wet-chemical method due to its quick and low-cost synthesis for the production of very pure, crystalline nanomaterials with a uniform size distribution.

Comparing cobalt ferrite to the analogous single-component metal oxides, the latter offers improved catalytic activity. This is due to the fact that metal oxides can be affected by both acid and alkali. However, ferrites are more chemically stable and are referred to as a popular heterogeneous catalyst owing to their magnetic separability. It can be recycled repeatedly without significantly losing its catalytic activity [7]. A strong dependence on diverse material responses over the cationic arrangement of the host material invites extensive investigations.

Jelokhani et al., prepared cobalt ferrite with carbon nanotube (CNT) and reduced graphene oxide (rGO) nanocomposites with a decrease in saturation magnetization, mean particle size, band gap, and recombination rate with the presence of rGO and CNT. The efficiency of the prepared  $\text{CoFe}_2\text{O}_4/\text{rGO}$  and CNT nanocomposites report a lower

degradation rate compared to the pure cobalt ferrite NPs [8]. Hassani et al. synthesized the combination of  $\text{CoFe}_2\text{O}_4/\text{rGO}$  nanocomposites through the thermal decomposition technique, in which  $\text{O}_2^-$  radicals contribute the major reactive species in the scavenger study. Also, the reusability of the nanocomposite decreases up to 22% after 5 consecutive cycles of degradation [9]. Similarly, the utilization of rGO with Ag-doped cobalt ferrite nanoparticles showed a degradation of about 93.25% compared to other pure cobalt ferrite and Ag-doped  $\text{CoFe}_2\text{O}_4$  nanoparticles. Thus, the MB dye was used to demonstrate a strong magnetic photocatalytic performance according to the literature [10]. There is an explosion of research on graphene oxide and reduced graphene oxide for use in photocatalysis. As a result, the present study encapsulates a detailed emphasis on the structural, magnetic, and photocatalytic insights of pure and graphene oxide-based cobalt spinel nanocomposites via experimental and theoretical simulations by density functional theory.

## 2 Materials and methods

### 2.1 Experimental method

Sol-gel combustion technique is employed to synthesize cobalt ferrite nanoparticles from the analytic-grade  $\text{Co}(\text{NO}_3)_2$  (Sigma-Aldrich Co. (99% purity), USA), and  $\text{Fe}(\text{NO}_3)_3$  (Sigma-Aldrich Co. (99% purity), USA). Similarly, graphene oxide (GO) is synthesized by modified Hummer's method with hydrogen peroxide as an oxidizing agent [11]. The detailed experimental procedure of GO preparation is illustrated in Figure S1. The synthesis of cobalt ferrite NPs usually incorporates polyvinyl alcohol (PVA) as an agglomeration reducer in the sol-gel combustion method [12].  $\text{Co}(\text{NO}_3)_2$  and  $\text{Fe}(\text{NO}_3)_3$  in a molar ratio of (1:2) were taken with appropriate quantities and dissolved in 100 mL of DI water, followed by the addition of citric acid as a chelating agent. The solution is stirred well to get a homogeneous solution. In addition to that, ammonia (1 M) is then added as a precipitating agent (pH~9). The solution is subsequently allowed to evaporate until the solution reaches the gel state. On continuous heating, the gel will result in combustion to produce a solid powder ash (cobalt ferrite nanoparticles). Consequently, the resulting cobalt ferrite and graphene oxide samples undergo solid-state synthesis reactions to form nanocomposites [13]. Finally, the pure cobalt ferrite ( $\text{CoFe}_2\text{O}_4$ ) and graphitic cobalt ferrite ( $\text{CoFe}_2\text{O}_4:\text{GO}$ ) NC samples are named CoF and CoF-GO, respectively. Further, a schematic representation of the formation of the nanocomposite is illustrated in Fig. 1.

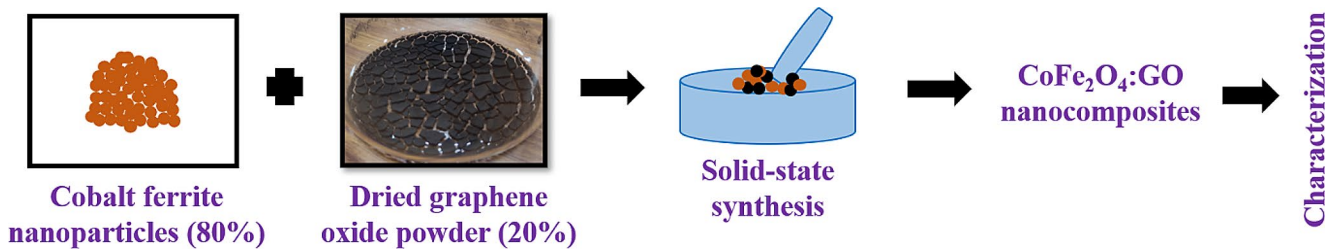


Fig. 1 Schematic illustration of CoFe<sub>2</sub>O<sub>4</sub>:GO nanocomposite preparation

## 2.2 Computational details

Pure and GO-doped spinel structures with  $3 \times 3 \times 3$  supercells were geometrically optimized using VASP simulations under 500 eV plane wave cut-off and  $2 \times 3 \times 3$  k-mesh for suitable convergence. The structural properties were evaluated with the help of a semi-empirical DFT+U approach to account for the relativistic effects (spin-orbit coupling) [14]. While standard Gaussian smearing with a smearing of 0.05 was preserved to achieve a constrained energy difference ( $1 \times 10^{-6}$  eV) between successive iterations. The phonopy package within VASP was utilized to examine the optical bandgap of dual compositions via the phonon density of states (PDOS).

## 2.3 Photocatalytic procedure

The degradation properties of the synthesized nanocomposites were evaluated using the methylene blue (MB) dye in an atmosphere of UV-visible light. A standard technique of photocatalyst preparation involves dispersing the catalysts (100 mg) in aqueous solution (100 mL) of MB dye (10 mg/L) [15]. An ultraviolet-visible spectrophotometer was used to measure the MB dye's absorption after exposure to light at regular intervals. The concentration of the MB dye solution was measured at its characteristic absorption peak of 664 nm using a UV-visible spectrometer. In order to facilitate photodegradation, a double-walled beaker reactor configuration was used. The reactor arrangement consisted of a jacket with lower glass hose connections on opposite sides and top-serrated hose connectors. A magnetic stirrer was utilized to stir the contents of the reactor. A UV light Xenon lamp ( $\lambda = 420$  nm, 86 W) was integrated into the setup and placed a maximum of 15 cm away from the reactor vessel as the light source. An exhaust fan was mounted on the reactor's back to reduce the amount of heat produced by the light.

## 3 Characterization studies

The following are the characterization studies carried out to analyze the CoFe<sub>2</sub>O<sub>4</sub>:GO nanocomposite samples. Bruker D8 Advance X-ray diffractometer with Cu- $k\alpha$  radiation (1.54056 Å) was utilized for X-ray powder diffraction measurements across a  $2\theta$  range of  $5^\circ$  to  $80^\circ$  using a step size of  $0.04^\circ$ . Shimadzu IRAffinity-1 (wavelength range: 400 to 4000  $\text{cm}^{-1}$ ) was used to observe FTIR. Jasco-UV-Visible spectrophotometer (V-670 PC) was employed for the UV-Vis-NIR spectroscopy and photocatalytic analysis. FE-SEM, EDAX, and Elemental mapping were carried out by Carl Zeiss Sigma 300 Field emission SEM and Zeiss SmartEDX analysis system, respectively. A vibrating sample magnetometer (VSM), Quantum Design, Dynacool-9 T is used to analyze the magnetic characterizations of the nanocomposites.

## 4 Results and discussion

### 4.1 Structural analysis

Spinel ferrites are a class of both soft and hard magnetic materials that derive their name due to their structural resemblance [16]. The term spinel corresponds to the cubic phase of compounds with a general  $\text{AB}_2\text{O}_4$  structure (A = divalent cations, B = trivalent cations). Such compounds display unique material properties (tunable electronic, optical, and magnetic response) and are classified into three different categories based on the cationic arrangement within the lattice [17]. While ideal spinel ferrites exist in the normal spinel structure, cationic substitutions on the other hand disrupt the periodicity to favor inverse or mixed spinel structures. As a result, standalone and CoFe<sub>2</sub>O<sub>4</sub>-based spinel ferrites have gained immense attention due to high magneto crystalline anisotropy and coercivity via inverse spinel ordering among a variety of spinel ferrites as shown in Fig. 2.

The inverse spinel structure of pure CoFe<sub>2</sub>O<sub>4</sub> displays a partial occupancy of  $\text{Co}^{2+}$ ,  $\text{Fe}^{3+}$ , and graphene oxide (GO) cations across the octahedral and tetrahedral positions respectively. According to Narang et al. [18], the cubic

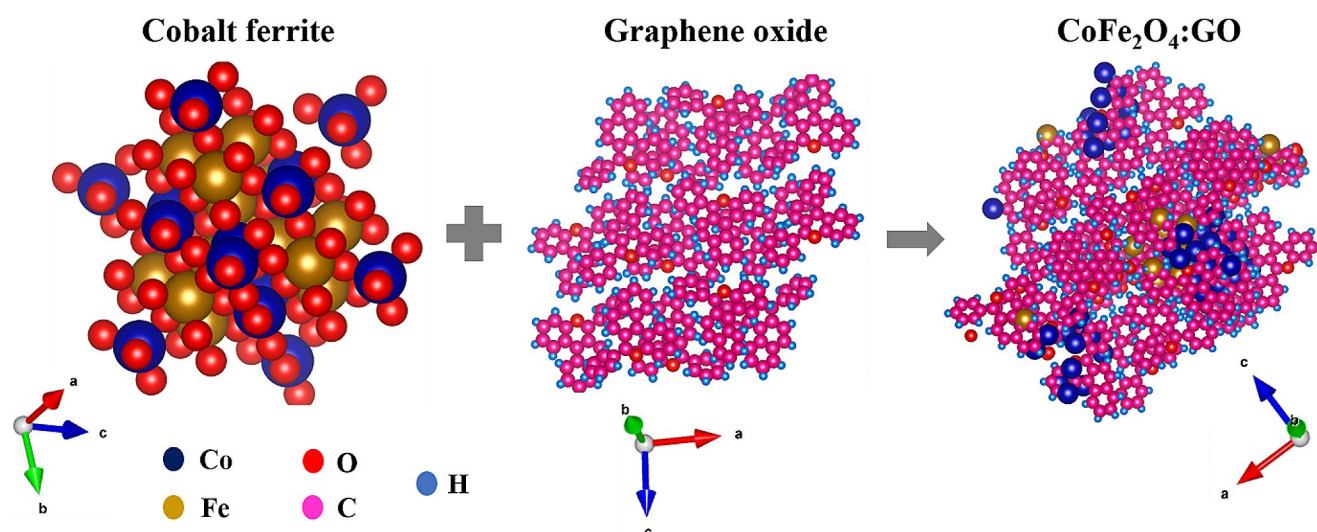


**Fig. 2** Pictorial representation of pure cobalt ferrite, graphene oxide, and  $\text{CoFe}_2\text{O}_4\text{:GO}$  nanocomposites

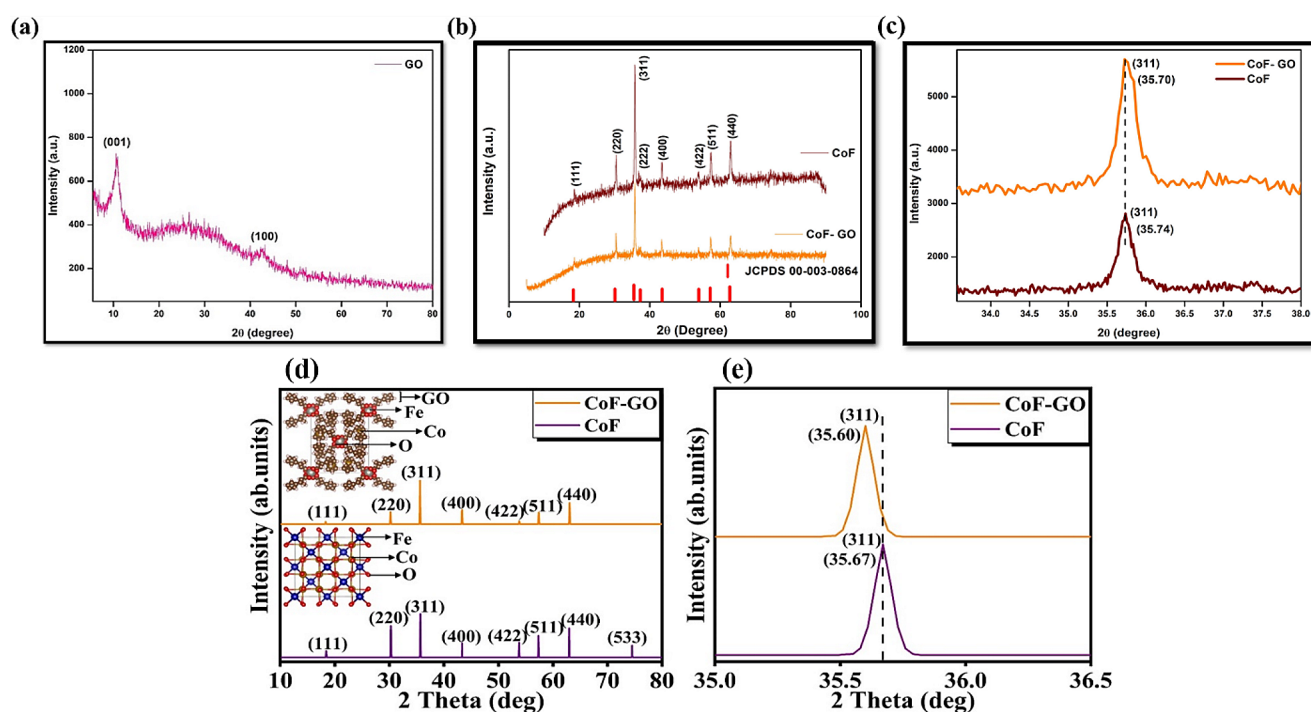


**Fig. 3** Experimental XRD profile of (a) Pure graphene oxide (GO), (b) Pure cobalt ferrite and graphitic cobalt ferrite nanocomposites, (c) Insight of (311) plane for  $\text{CoFe}_2\text{O}_4\text{:GO}$  NCs, (d) DFT simulated

symmetry of spinel ferrites comprises 8 divalent cations, 16 trivalent cations, and 32 oxygen anions respectively. As a result, the inverse spinel structure of pure and GO-modified  $\text{CoFe}_2\text{O}_4$  compound, the 4 divalent  $\text{Co}^{2+}$  cations, and GO occupy the 16 available B-site while the 16 trivalent  $\text{Fe}^{3+}$  cations partially occupy the 8 available locations across the A-site and B-site within the lattice. While the crystal structure of the composite (in Fig. 2) was obtained by merging the individual structures of pure  $\text{CoFe}_2\text{O}_4$  and graphene oxide

XRD pattern of  $\text{CoFe}_2\text{O}_4$  and GO-doped  $\text{CoFe}_2\text{O}_4$ , and (e) peak-shift of (311) prominent peak of dual compositions

into a single entity using the crystallographic information of the compounds via Vienna ab initio Simulation Package (VASP) and VESTA software, the phase purity and symmetry of pure and GO modified  $\text{CoFe}_2\text{O}_4$  compounds were validated using the X-ray diffraction analysis respectively.

As a result, the X-ray diffraction pattern of the synthesized powder samples using the sol-gel auto-combustion route shows the expected inverse spinel structure [19]. As the growth rate continues to exceed the nucleation rate,

**Table 1** Experimentally analyzed structural parameter of pure and GO-doped  $\text{CoFe}_2\text{O}_4$  spinel nano-ferrite

Sample code	D (nm)	a (Å)	d (Å)	V (Å <sup>3</sup> )	$\epsilon * 10^{-4}$	$\delta * 10^{14} \text{ m}^{-2}$	$L_A$ (Å)	$L_B$ (Å)
CoF	27.78	8.326	2.121	577.18	12.72	13.73	3.605	2.943
<b>CoF-GO</b>	40.25	8.338	2.124	579.69	8.79	6.58	3.610	2.947

**Table 2** DFT simulated lattice parameter of pure and GO-doped CoF compositions

Sample code	DFT simulated lattice parameter			Prior experimental evidence	% Error of DFT simulated parameters with respect to the prior experimental report	Ref
	a (Å)	b (Å)	c (Å)			
CoF	8.328	8.328	8.328	8.354	0.311	[26]
CoF-GO	8.339	8.339	8.339	-	-	

the slow mixing of  $\text{NH}_4\text{OH}$  leads to larger-sized particles. Figure 2 depicts the pictorial representation of pure cobalt ferrite, graphene oxide, and  $\text{CoFe}_2\text{O}_4$ :GO nanocomposites. Figure 3 (a-c) illustrates the experimental approach to structural investigation via XRD diffractograms of dual nanocomposites.

The XRD reflections of host and derived  $\text{CoFe}_2\text{O}_4$  spinel nanoferrites showcase complete phase formation (JCPDS 00-003-0864) devoid of impure secondary phases as shown in Fig. 3 (b), while the diffraction peak of graphene oxide at  $2\theta=10.59^\circ$ , ascribed to the crystallographic planes (001) (as shown in Fig. 3(a)) respectively [20]. The disappearance of the GO peak corresponding to (001) (as shown in Fig. 1(a)) indicates the surface overlap of  $\text{Fe}_3\text{O}_4$  nanoparticles over the GO surface with a consequent rise in the interlayer spacing between GO sheets. The higher proportion of  $\text{CoFe}_2\text{O}_4$  interferes with the diffraction pattern of GO by masking its peaks or broadening the peaks resulting in the absence of the characteristic peak of GO [9]. The d-spacing of the composite phase is slightly higher (2.124 Å) than the pure  $\text{CoFe}_2\text{O}_4$  NPs (2.121 Å) due to the interlayer spacing of GO with the presence of oxygen-containing functional groups (hydroxyl and epoxide groups), causing the layers to be more separated compared to the pristine graphene. Also, the interactions between the composite materials ( $\text{CoFe}_2\text{O}_4$  and GO) can lead to the intercalation or adsorb the nanoparticles into the GO sheets. This interaction can cause the GO layers to expand further, increasing its interplanar spacing.

Annealing reduces lattice imperfections and stresses, which leads to crystallite coalescence and increases the average size of the nanoparticles [21]. Thus the experimentally evaluated structural parameters of the resultant nanocomposites are tabulated (Table 1) via requisite formulae used in our previous work [22]. The increase in lattice constant and hopping length (as shown in Table 1) originates from the inhabiting nature of graphene oxide within cobalt ferrite nanoparticles. A gradient among the grain size distribution invokes robust reliability of different compositional

stoichiometry upon the final adiabatic temperature during the combustion reaction.

While experimental analysis is essential to examine the practically synthesized compositions, however, heavy reliability upon the experimental conditions and processing techniques often invites under/overfit of the structural parameters. The afore-response is critical with spinel nanoferrites with strong structural dependent material properties. As a result, theoretical insight via state-of-the-art DFT analysis is vital to support the experimental outcomes with constrained approximations. The quantum many-body self-consistent (SCF) calculations at the microscopic scale in DFT allow the evaluation of diverse structural and other desirable characteristics with improved accuracy. Among different spinel ferrites,  $\text{CoFe}_2\text{O}_4$  is well-known for extensive applications in compliance with our prior discussion. Furthermore, graphene oxide (GO), on the other hand, is a promising candidate for photocatalytic applications with desirable dual-band positioning. Besides pure  $\text{CoFe}_2\text{O}_4$ , GO-doped  $\text{CoFe}_2\text{O}_4$  preserves structural invariance as shown in Fig. 3.

The X-ray diffractograms with a prominent (311) reflection illustrate a characteristic polycrystalline cubic inverse spinel structure devoid of impurities with  $Fd\bar{3}m$  and  $Pa\bar{3}$  symmetry for dual compositions ( $\text{CoFe}_2\text{O}_4$  (CoF) and GO-doped  $\text{CoFe}_2\text{O}_4$  (CoF-GO)) as shown in Fig. 3(d-e) respectively [23]. The coupling of GO with the host material on the other hand minimizes the characteristic (001) and (100) reflections of GO due to the exfoliation of GO and the feeble peak intensity relative to parent composition as observed experimentally in Fig. 3(b) respectively [24, 25].

While the geometrical parameters of host spinel nanoferrites preserve invariance with present and prior experimental reports, GO substitution on the contrary induces lattice expansion due to prevalent cationic migrations between distinct interstices as shown in Table 2. The resultant lattice strain due to energy landscapes among dual interstices constitutes disparate physiochemical responses.

The fcc lattice of pure and doped CoF inverse spinel nanoferrites with dual-site (tetrahedral and octahedral)  $O^{2-}$  coordination enhances the specific surface area (SSA) for improved charge storage capacity. Facile charge transfer pathways between two tetrahedral interstices concern the ionic displacement via a blend of vacant octahedral and triangular faces of the tetrahedron. The aggregate effect accords with the transition state of the diffusion mechanism. The distorted edge and O-Fe<sub>3</sub>-Co corner sharing trigonal pyramid are responsible for a low migration barrier and a resultant short percolation channel due to less intense (400) and (422) indexed peaks [23]. However, a curtail in (422) peak intensity with a preserved congruency across (400) relative to their host counterpart indicates a significant tetrahedral contribution of GO with Fe cations over octahedral analog. The unified impact of GO substitution further aids a rapid charge transfer via a subsequent curtail in the electronic bandgap, which expands their gateway into the technological facets of energy storage.

## 5 FTIR analysis

Fourier transform infrared spectroscopy detects the presence of functional group elements in the nanocomposites of graphitic-cobalt ferrites. In the spectrum of CoFe<sub>2</sub>O<sub>4</sub>:GO, a characteristic strong peak at 536 and 549 cm<sup>-1</sup> is identified with other weak peaks that fit well with those reported for graphene composites. Figure S2. clearly shows the stretching and vibrational modes of the synthesized nanocomposites [27]. The stretching vibrations of iron oxides were detected in the range of 536.4 and 549.4 cm<sup>-1</sup>. It confirms the formation of ferrites in the NCs. The stretching vibrations of C-O are observed at 1064.2 cm<sup>-1</sup>. The existence of bands at 1603.2 and 1625.2 cm<sup>-1</sup> assures the H-O-H and O-H stretching vibration of H<sub>2</sub>O and carboxylic acid [28]. The hydrogen bonding between the silanol group causes a stretching vibration of H<sub>2</sub>O and hydroxyl, which causes the

band at 3232.8 cm<sup>-1</sup>. The disappearance of bands at 1064.2 and 3232.8 cm<sup>-1</sup> is due to the addition of oxygen-containing functional groups of graphene oxide in the nanocomposites.

## 6 UV-Vis-NIR

The UV-Vis transmittance spectra from Fig. 4 (a & b) show the optical spectra for the prepared bare CoFe<sub>2</sub>O<sub>4</sub> and CoFe<sub>2</sub>O<sub>4</sub>:GO nanocomposites. The optical band gap energy of the synthesized ferrites under study was estimated using absorbance in UV-Vis spectral measurements in the UV-Vis-NIR range [29]. The d-d transitions of Fe<sup>3+</sup> are represented by a broad absorption range (300–600 nm) in the visible spectrum region in the UV-Vis-NIR spectra. CoFe<sub>2</sub>O<sub>4</sub>:GO NCs and bare CoFe<sub>2</sub>O<sub>4</sub> showed direct band gap values of 1.12 eV and 1.10 eV, respectively. It is clear that, as the crystalline size increased from 27.78 to 40.25 nm, the band gap energy decreased from 1.12 to 1.10 eV for the prepared nanocomposites. The band gap energy varied with an inverse relationship with their sizes. Similarly, the bandgap values obtained from the DFT simulation are close to the observed values with a difference of about  $\pm 0.05$  eV.

More atoms and overlapping atomic orbitals are present when the crystalline size is large. As a result, more bonding and antibonding molecular orbitals will result in a smaller bandgap. According to the absorption coefficient ( $\alpha$ ), Tauc's graph is used to determine the energy band gap ( $E_g$ ) of the nanocomposites by the relation (Eq. 1) [30].

$$\alpha h\nu = A(h\nu - E_g)^n \quad (1)$$

Where “n” is a value ( $n = 1/2$ ) that relies on the type of the electronic transition, “ $h\nu$ ” is the energy of an incident photon, and “A” is a constant that varies depending on the type of transition.

Thus, by plotting  $(\alpha h\nu)^2$  Vs the incident photon energy ( $h\nu$ ) graph, as shown in Fig. 5, and extrapolating the straight

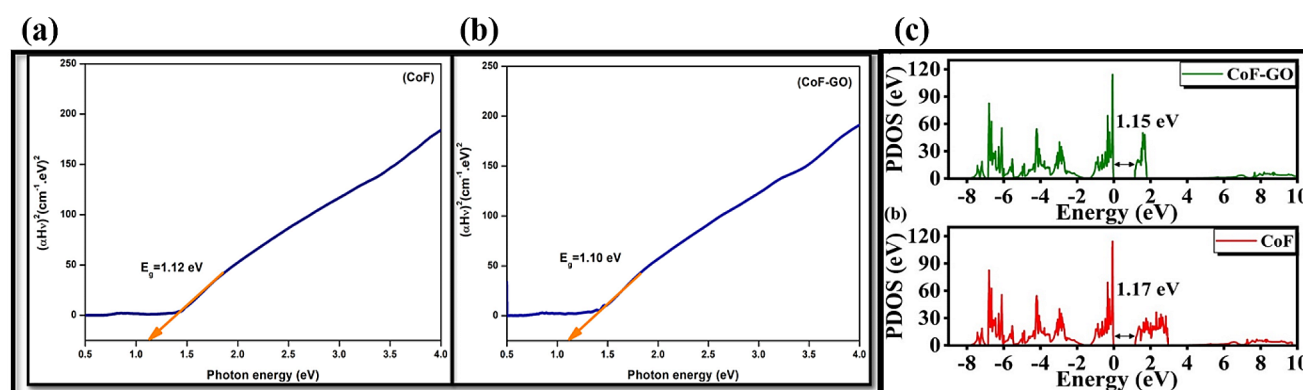


**Fig. 4** Optical bandgap energy values for (a) pure cobalt ferrite (b) CoFe<sub>2</sub>O<sub>4</sub>:GO NCs, and (c) DFT simulated Phonon density of states (PDOS)

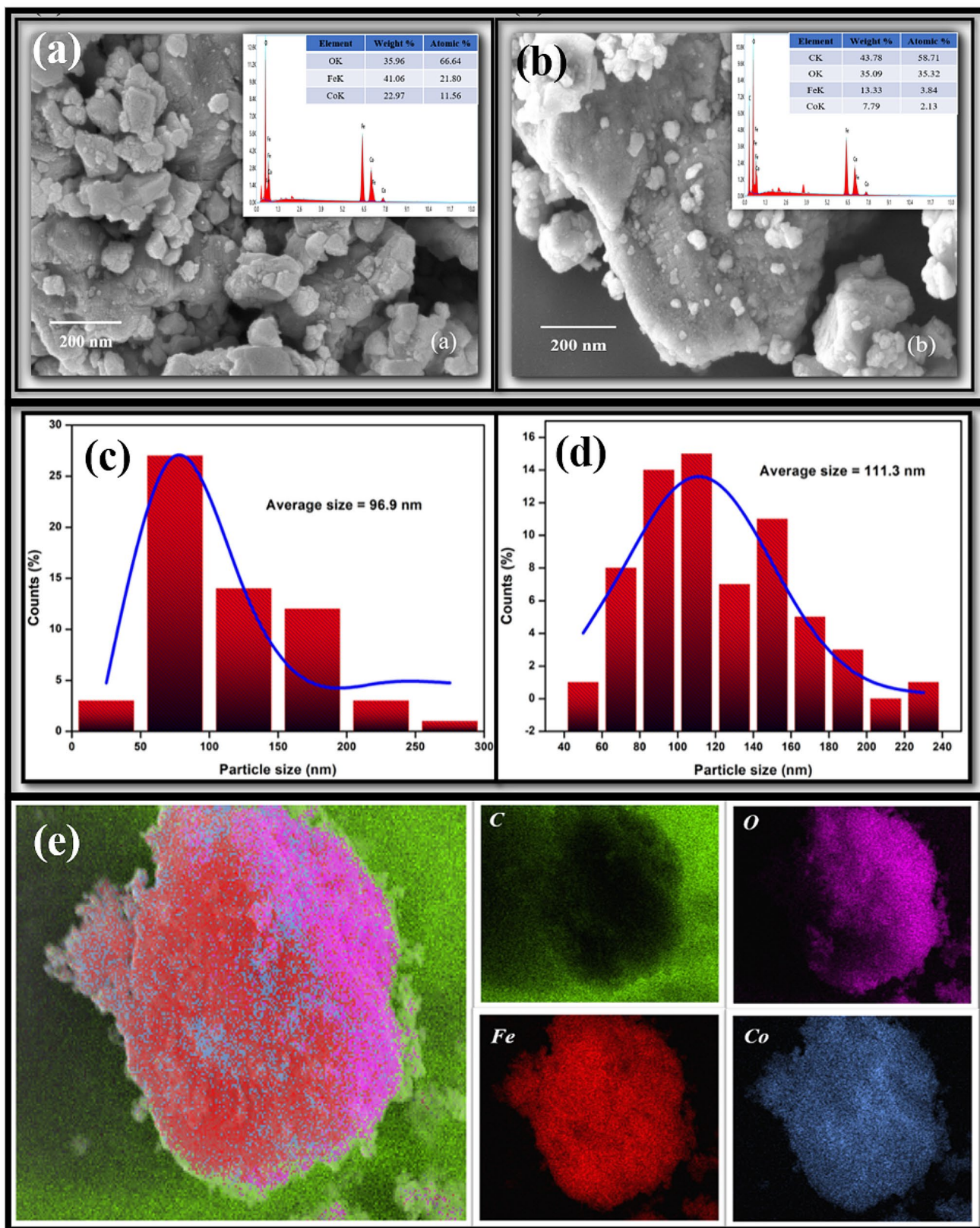


**Fig. 5** FE-SEM images (a & b) pure cobalt ferrite and CoFe<sub>2</sub>O<sub>4</sub>:GO NCs, Size histogram graph of (c & d) pure cobalt ferrite and CoFe<sub>2</sub>O<sub>4</sub>:GO NCs, and (e) Elemental distribution of CoFe<sub>2</sub>O<sub>4</sub>:GO nanocomposites

line to  $(\alpha h\nu)^2 = 0$ , the energy gap value can be determined. The optical properties can be determined by some factors like energy gap, dopant concentration, the lattice constant, crystalline size, oxygen deficiency factors, and surface roughness. The change in  $E_g$  values may result from interactions among free carriers and ionized impurities or could be caused by the changes between the free charge carriers [8].

In ferrite nanoparticles, the O-2p orbital and the Fe-3d orbital create the valence band and conduction band, respectively. The observed decrease in optical energy gap is due to the increase in electron-electron-hole charge separation, Fermi level of the supported metal, and increased catalytic ability [31]. In compliance with our prior claims, an increase in the specific surface area with GO-doped compositions favors high photocatalytic activity. A desirable absorption of cations and anions by GO-doped composition relative to their parent counterpart constitutes a fundamental and requisite pre-condition for an ideal photocatalyst. While the magnitude of optical absorption strongly relies upon the incident photon energy and the material's optical bandgap [32]. A relatively small optical gap state of the CoF-GO matrix over their parent counterpart affirms our prior claims using phonon density of states (PDOS) in Fig. 4 (c).

From the vault of the structural landscape, a decrease in the optical bandgap of the GO-doped composition (in Fig. 4 (c)) also dictates a strong correlation with the grain size of the resultant composition. An increase in the crystallite size imparts an inverse impact on the optical bandgap of the resultant spinel ferrite. The afore-hypothesis goes in agreement with the works of Agrawal et al. [33]. The study projects a consequent effect due to an inverse dependency of the crystallite size to the optical bandgap of the resultant spinel nano ferrite based on Brass's effective mass model [34, 35].

## 7 FE-SEM & EDX analysis

Field emission scanning electron microscopy (FESEM) photographs of cobalt ferrite with graphitic nanocomposites are observed with a resolution of 200 nm as shown in Fig. 5 (a & b). The prepared nanocomposites were well agglomerated with a uniform distribution [36]. The growth of agglomerated nanoferrites is due to the higher calcination temperature practiced during the synthesis of NCs. The surface of the prepared nanocomposite samples appeared to be in agglomerated nanoplate-like morphology as shown in Fig. 5 (a & b). The particles are separated as the crystalline size increases by incorporating graphene oxide [37]. The aggregation of the particles has erratic forms and varying sizes due to the combustion reaction. A clear agglomeration image of the nanocomposites is observed at the resolution of 200 nm with the maximum particle size of about 96.9

and 111.3 nm for bare cobalt ferrite and cobalt ferrite with graphene oxide nanocomposites, respectively (Fig. 5 (c & d)). This agglomeration may be due to the non-addition of surfactant during the magnetic material synthesis process. Also, some additional images of the prepared nanocomposites are incorporated in supplementary information (Figure S2).

By the composition of the nanocomposite, the particle size appears to rise virtually linearly, which most likely speeds up the coalescence process and causes an increase in particle size [38]. Additionally, it indicates that the two important parameters like time and annealing temperature can result in an increase or decrease in particle size.

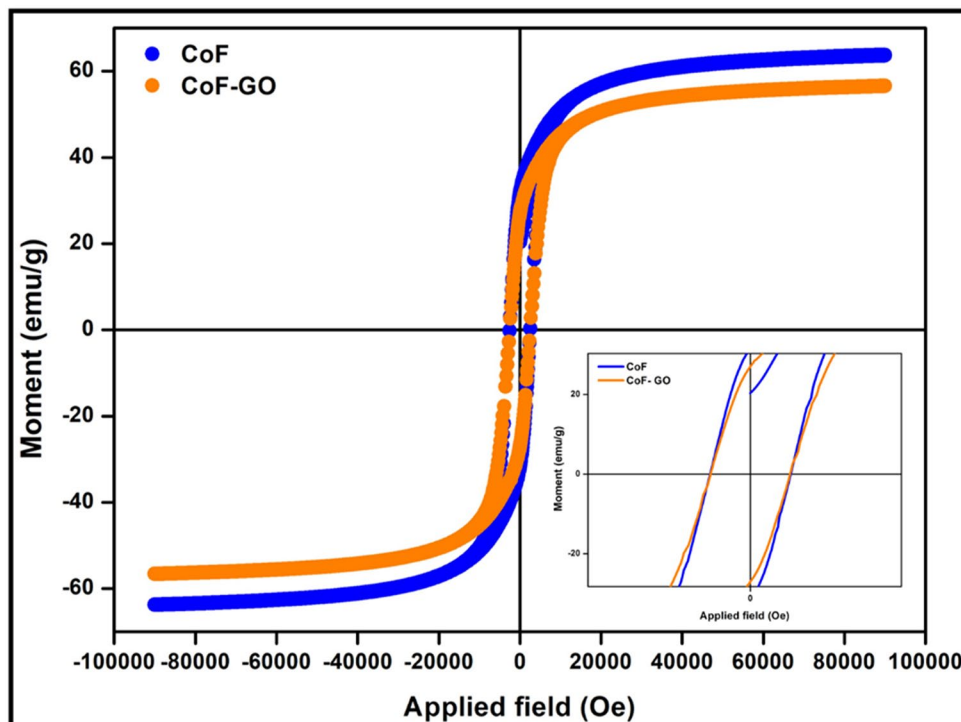
In energy dispersive X-ray microanalysis (EDX), the composition of elements in  $\text{CoFe}_2\text{O}_4$ :GO NC samples was measured and their atomic % was observed to be 58.71, 35.32, 3.84, and 2.13 for C, O, Fe, and Co, respectively. For bare  $\text{CoFe}_2\text{O}_4$ , the atomic % was found to be 66.64, 21.80, and 11.56% of O, Fe, and Co, respectively. The exact stoichiometry of  $\text{CoFe}_2\text{O}_4$  and  $\text{CoFe}_2\text{O}_4$ :GO NCs was also confirmed by this measurement. The extra atomic % of C is found due to the carbon coating of EDX analysis. Figure 5 (e) shows the EDX spectrum for the prepared nanocomposites. The spatial distribution of elements in the nanocomposites is seen in the elemental mapping. The differential color exhibits the presence of all the elements in the NCs.

## 8 Magnetic analysis

Spinel nanoferrites made of cobalt are a well-known contender with promising magnetic properties (Fig. 6). The level of magnetic response can be revealed by the distribution in the binary interstice and the nature of cations [39]. Strong magnetic characteristics are caused due to the tetrahedral occupancy of  $\text{Fe}^{3+}$  cations with ferro and antiferromagnetic ordering, and a double exchange between  $\text{Fe}^{3+}$  and  $\text{Co}^{2+}$ , respectively. Further, zero field cooled (ZFC) and field cooled (FC) measurements were performed at both low (3 K) and high temperatures (800 K) to ensure that the nanocomposite samples were in the ferrimagnetic condition (Fig. 7). In ZFC measurements, the sample is cooled to a low temperature of 3 K under a magnetic field of 0.01T and then magnetization is recorded while heating the sample. In FC measurement, the sample is cooled from high temperature to low temperature in the presence of the magnetic field. The observation of splitting between the ZFC and FC curves is due to the presence of magnetic anisotropy [40]. Thermomagnetic curves show that the Curie transition ( $T_c$ ) is above the room temperature. Table 3 shows the  $T_c$  of both samples and was estimated by taking the first-order derivative of the thermomagnetic curve [41].



**Fig. 6** MH loop for pure  $\text{CoFe}_2\text{O}_4$  and  $\text{CoFe}_2\text{O}_4$ :GO NCs



According to Table 3, an appreciable saturation magnetization ( $M_s$ ) for pure  $\text{CoFe}_2\text{O}_4$  is the inverse spinel cationic arrangement, super-exchange interactions, and magnetic anisotropy [51]. A heterogeneous  $\text{Fe}^{3+}$  distribution ( $\text{Fe}^{3+}/\text{Co}^{2+} > 1$ ) within the octahedral site increases the octahedral magnetic moment ( $\mu_{\text{octa}}$ ) with a proportional decline in the magnetic moment of the tetrahedral site ( $\mu_{\text{tetra}}$ ) which constitutes a cumulative increase in the net magnetic moment ( $\mu_B$ ) of the resultant composition according to Eq. 2 shown below:

$$\mu_B = \mu_{\text{octa}} - \mu_{\text{tetra}} \quad (2)$$

A Langevin function can be used to define the specific structure of the magnetization curve in the MH loop (Fig. 6), which is dependent on the particle volume. The cationic rearrangement and rigid ionic bonds within inverse spinel structures also follow a congruent footstep to the material's magnetic response [42]. Comprehensive magnetization of  $\text{CoFe}_2\text{O}_4$  nanoferrites originates due to low magnetic anisotropy and a proportional dependency upon the Co-Fe bond strength with super-exchange  $\text{Co}^{2+}\text{-O-Fe}^{3+}$  over Co-Co and Fe-Fe counterparts [43, 44]. Magnetic measurements like saturation magnetization ( $M_s$ ), coercivity ( $H_c$ ), remanent magnetization ( $M_r$ ), magnetic moment ( $n_B$ ) in terms of Bohr magneton, and squareness loop ratio ( $M_r/M_s$ ), and magnetic moment ( $n_B$ ) are calculated from the formulae used in our previous work and reported in Table 3.

The total of all of the unpaired spins of the cations produces saturation magnetization. The distance between two metal ions at distinct sites and the oxygen ion that connects them determines the exchange force or negative interaction between those moments [45]. The interatomic distances are the shortest and the interaction is highest at an angle of  $180^\circ$  [46]. Additionally, it has been noted that synthesis parameters have an impact on the saturation value. For instance,  $\text{CoFe}_2\text{O}_4$  NPs produced at  $\text{pH} \sim 11$  displayed greater  $M_s$ . This is explained by the fact that the crystallinity of the spinel nanoferrites directly correlates with the magnetic nanoparticle's energy in a field.

The cation distribution and the size impact both contribute to the observed decrease in saturation magnetization. Since oxygen anions and cations are close together and the inclination within A-O-B ions falls between  $125^\circ$  and  $154^\circ$ , spinel ferrites have high A-B interaction energies [47]. Consequently, the surface disorder and canted spins caused by an increase in the pores, lattice strain, and interatomic distance of the graphene oxide material are primarily responsible for the reduction in magnetization.

The coercivity broadens with size rapidly, reaching a maximum value, and subsequently declines with particle size, according to the Gaussian fit. There are two possible explanations for the drop at larger sizes. First, it can be a result of the anticipated transition from a single domain to multidomain behavior as size increases. Second, an interaction of thermal energy and surface anisotropy. Due to the importance of anisotropy in the formation of domains and

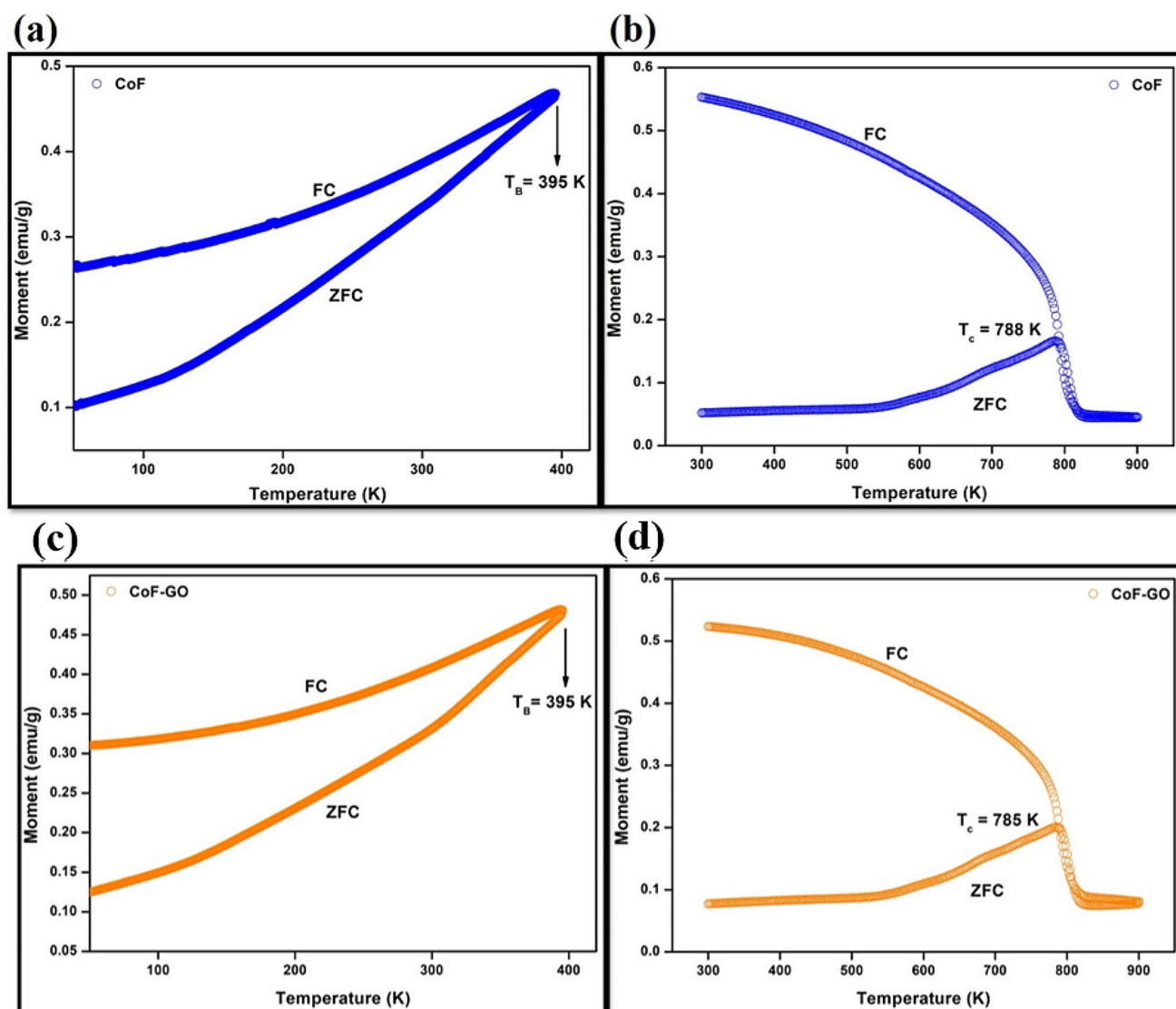


**Fig. 7** Illustration of (a & c) Blocking temperature and (b) Curie temperature of pure and  $\text{CoFe}_2\text{O}_4$ :GO nanocomposites

**Table 3** Magnetic response of pure and GO-coupled  $\text{CoFe}_2\text{O}_4$  spinel ferrites

Composition	DFT simulated magnetic response (present work)		Prior experimental reports		Ref
	Magnetic moment ( $\mu_B$ ) (emu/g)	Saturation magnetization ( $M_s$ ) (emu/g)	Saturation magnetization ( $M_s$ ) (emu/g)	Percentage error (%)	
CoF	3.48	78.15	78.70	0.69	[50]
CoF: GO	2.72	61.28	-	-	-

the importance of its control in the development of magnetic materials for applications in technology, the concept of anisotropy is of great practical relevance. The Law of Approach to Saturation (LAS) can be used to evaluate the sample's effective anisotropy constant ( $K_{\text{eff}}$ ) in spinel ferrites [48, 49].

A sizeable magnetic behavior of  $\text{CoFe}_2\text{O}_4$  spinel ferrite occurs due to 3d-orbital contributions by the respective cations within the interstice [48]. The estimated magnetic

response of the host and GO-coupled spinel ferrites are reported in Table 4.

Meanwhile, GO-coupled spinel ferrite on the contrary no longer favors the ferrimagnetic ordering of spins due to a partial transfer of  $\text{Fe}^{3+}$  ions to the tetrahedral interstice with their resultant GO occupancy at the octahedral sites, which in compliance with Eq. 2 curtails the net magnetic moment ( $n_B$ ) of the overall composite. Besides a more critical aspect of the former consequence originates due to surface effects.

**Table 4** Magnetic measurements of pure CoFe<sub>2</sub>O<sub>4</sub> and CoFe<sub>2</sub>O<sub>4</sub>:GO NCs

Sample Code	M <sub>s</sub> (emu/g)	H <sub>c</sub> (Oe)	M <sub>r</sub> (emu/g)	(M <sub>r</sub> /M <sub>s</sub> )	n <sub>B</sub> (μ <sub>B</sub> )	T <sub>c</sub> (K)
CoF	63.74	2533.94	31.60	0.49	4.103	788
CoF: GO	56.60	2526.27	26.81	0.47	3.644	785

A recent study by Mariosi et al. [52] signifies the role of surface effects towards reduced magnetization of oxides spinel ferrites. The surface coupling of magnetically inactive layers or spin canting of such oxides in the bulk volume of the crystallites dictates a direct influence upon saturation magnetization [53]. According to the study of Ditta et al. [54], such a synergetic effect transforms the orientation of the magnetic moment with a consequent decrease in the magnetization of the composite matrix. In compliance with the outcomes of our present study (as shown in Table 4), a decline in the net magnetic moment and the resultant magnetization of about 21.58% among GO coupled spinel composites relative to host counterpart occurs due to a decrease in the magnetic anisotropy. A recent study by Narang et al. [18] suggests a strong correlation of magnetic anisotropy (K<sub>eff</sub>) with crystallite size, bulk anisotropy, and size anisotropy (K<sub>surface</sub>) according to Eq. 3.

$$K_{eff} = K_{bulk} + 6 \frac{K_{surface}}{d} \quad (3)$$

A large particle size (D=40.25 nm) among GO-coupled composition (according to Table 1) with a decrease in the bulk anisotropy (K<sub>bulk</sub>) due to reduced Fe<sup>3+</sup> concentration consequently curtails the magnetic anisotropy. The former observation agrees with the outcomes of Wang et al. [55], which dictates an inverse interplay between crystallite size and the magnetic response of the spinel composite. Meanwhile, GO-coupled spinel composites resist the penetration of magnetic field lines due to the heterostructural magneto dielectric interface, which induces a fractional paramagnetic characteristic with a resultant decrease in saturation magnetization, respectively.

## 9 Photocatalytic analysis

One of the outstanding characteristics of spinel ferrite NPs that make them suitable for wastewater treatment is that they lack magnetic dipoles, which are present in superparamagnetic materials. MB pigment (C<sub>16</sub>H<sub>18</sub>N<sub>3</sub>SCl) was used in the aqueous solution for the photodegradation studies [56]. By removing MB from water at various initial concentrations, the functionalization of prepared photocatalysts was investigated. After 120 mins of darkness, the dye reached its adsorption equilibrium in the presence of the required catalyst loading. Using a UV JASCO (V-570) spectrophotometer

with λ<sub>max</sub> = 653 nm, the concentration of inert MB dye was measured. The degradation started (t=0) under the irradiation of visible light when the light source was turned on, and the photodegradation reaction thereafter continued. It is really intriguing how drastically passive CoFe<sub>2</sub>O<sub>4</sub> transforms into an extremely efficient catalyst for the breakdown of MB dye when exposed to visible light when combined with graphene [57].

Methylene blue is extensively utilized in diverse industrial applications such as textile dyeing, biological sample staining, and medicinal purposes. However, inadequate management of its usage can result in substantial environmental contamination. Moreover, MB dye risks aquatic organisms and ecosystems if it enters water bodies. Therefore, a comprehensive understanding of its environmental behavior, degradation pathways, and potential remediation methods is crucial to mitigate its impact. The selection of MB dye was motivated by its widespread use, potential environmental and health implications, and the necessity to devise effective mitigation strategies. Addressing these issues can significantly enhance scientific knowledge and practical applications in environmental conservation and public health (Fig. 8).

To calibrate the methylene blue concentration for quantifying its amounts in water samples, we prepared a series of standard solutions with known concentrations of methylene blue. Using a UV-Vis spectrophotometer, we measured the absorbance of these standards at the maximum absorption wavelength of methylene blue (around 665 nm). We then generated a calibration curve by plotting the absorbance values against the known concentrations, establishing a linear relationship. This calibration curve allowed us to determine the concentration of methylene blue in unknown water samples by measuring their absorbance and interpolating the corresponding concentrations from the curve. For enhanced reproducibility, we ensured precise preparation of standard solutions, consistent use of the spectrophotometer, and proper calibration of the instrument. Before UV-visible light irradiation, the catalyst containing dye solution was placed in the dark condition for one hour to achieve the adsorption-desorption isotherm. Under visible light irradiation, the blank test and the control test were carried out using GO and CoFe<sub>2</sub>O<sub>4</sub>, which could not effectively remove MB dye (Fig. 9).

The MB solution's color gradually changed from blue to light blue to finally twisted to colorless, which may be related to the alienation of the chromophoric unit. The

**Fig. 8** Probable photocatalytic degradation mechanism for  $\text{CoFe}_2\text{O}_4$ :GO nanocomposites against MB dye degradation

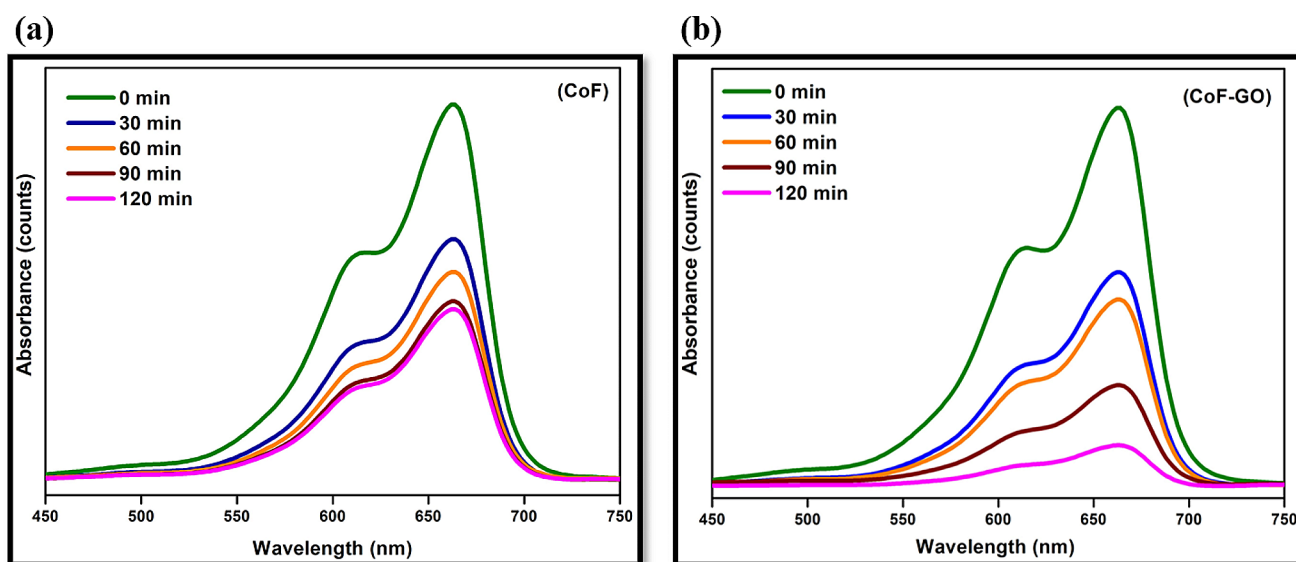
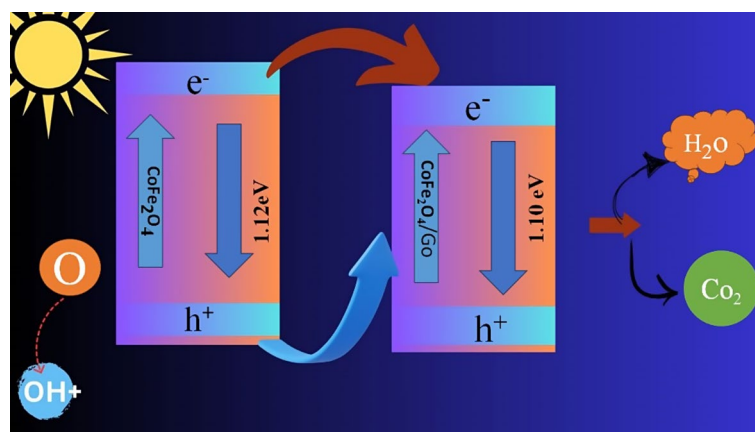


**Fig. 9** UV (degradation) spectra of methylene blue (MB) dye

photocatalytic efficiency was calculated using the formula used in our previous work [22]. Figure 10 presents the kinetic plot of  $(C_0/C_t)$  Vs irradiation time (mins), analyzing the degradation of methylene blue and assessing the photocatalytic performance of the synthesized materials. The results clearly indicate that the photocatalysts followed pseudo-first-order kinetics. In Table 5, the rate constant values ( $K_{app}$ ), correlation coefficients ( $R_2$ ), and maximum dye degradation efficiencies for  $\text{CoFe}_2\text{O}_4$  and  $\text{CoFe}_2\text{O}_4$ :GO nanocomposites were provided. As per the observed results, the rate constant for the  $\text{CoFe}_2\text{O}_4$ :GO composites was notably higher than pure  $\text{CoFe}_2\text{O}_4$  nanoparticles.

As graphene oxide is incorporated, the surface area increases, and there is less electrons-holes recombination due to electrical interaction in  $\text{CoFe}_2\text{O}_4$ :GO NCs, which causes the degradation of MB dye to occur at a faster rate [58]. Since there are more surfaces for the dye to adsorb on, the materials with small sizes have high surface areas, which facilitate surface reactions with hydroxyl (OH)

radicals produced on catalyst surfaces. As a result, the degradation efficiency for pure cobalt ferrite nanoparticles and  $\text{CoFe}_2\text{O}_4$ :GO nanocomposites are observed to be 53.10 and 87.74%, respectively. Figure 9 gives the ultraviolet-visible absorption graph of MB dye +  $\text{CoFe}_2\text{O}_4$ :GO NCs (from 0 to 120 mins).

The  $\text{CoFe}_2\text{O}_4$  and GO nanocomposites exhibit superior photocatalytic performance compared to its bare counterparts due to enhanced light absorption, efficient charge separation, and improved stability. Light is essential as it initiates the photocatalytic process by generating electron-hole pairs, which are then utilized in redox reactions to degrade pollutants or facilitate other desired chemical transformations. Based on previous findings and illustration in Fig. 10 (d), the degradation mechanism of the  $\text{CoFe}_2\text{O}_4$ :GO heterostructure under visible light involves the generation of electron-hole pairs upon stimulation of  $\text{CoFe}_2\text{O}_4$  and GO. Electrons migrate to the conduction band of  $\text{CoFe}_2\text{O}_4$ , leaving behind holes in its valence band. Meanwhile, electrons

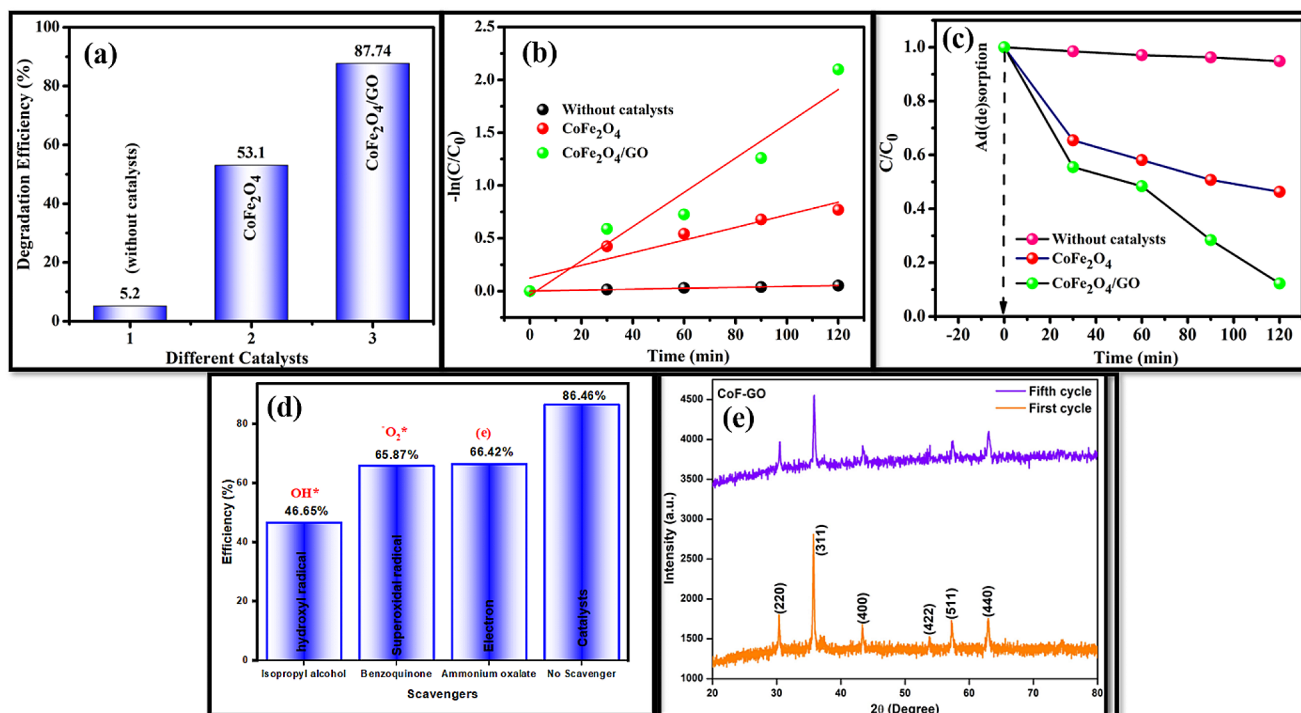


**Fig. 10** **a** Degradation efficiency with and without catalysts, **b**  $\ln(C/C_0)$  Vs time graph, **c** Representation of  $(C/C_0)$  Vs time graph, **d** Methylene Blue catalytic performance with different scavengers with the presence

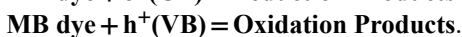
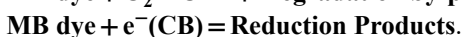
of CoF-GO photocatalyst, and **e** XRD patterns of CoF-GO nanocomposite for the first and fifth cycles of the degradation process

**Table 5** Photocatalytic degradation and rate constant values of pure and GO-incorporated nanocomposite

Photocatalysts	$K_{app}(\text{min}^{-1})$	$R^2$	Degradation (%)
CoF	0.0059	0.8917	53.10
CoF: GO	0.0162	0.9488	87.74

and holes in GO can diffuse into  $\text{CoFe}_2\text{O}_4$ , establishing a p-n heterojunction between the p-type GO and n-type  $\text{CoFe}_2\text{O}_4$  photocatalysts. During this process, photo-induced electrons transfer from  $\text{CoFe}_2\text{O}_4$  to GO, while holes transfer from GO to  $\text{CoFe}_2\text{O}_4$ , establishing a Fermi-level equilibrium. This creates an internal electric field (E) at the interface of GO and  $\text{CoFe}_2\text{O}_4$ , effectively separating the photo-induced electron-hole pairs. The photo-excited electrons participate in reactions leading to the formation of reactive oxygen species such as  $\cdot\text{O}_2^-$  and  $\cdot\text{OH}$ , which subsequently react with MB dye in solution. Further, the presence of the p-n heterojunction in  $\text{CoFe}_2\text{O}_4$ :GO NC enhances the photocatalytic efficiency compared to pure  $\text{CoFe}_2\text{O}_4$  and GO.

The photocatalytic mechanism pathway is described in below;



For practical applications, recycling and reusing a photocatalyst in the subsequent degradation cycle of organic pollutants is always advantageous and more cost-effective. To check the stability and useability of the prepared nanocomposite (CoF-GO), the material undergoes XRD analysis after five cycles of the degradation process. Figure 10 (e) demonstrates that the XRD spectra do not show any extra peak even after five cycles of degradation, revealing that the samples are highly stable. Also, in Fig. 10 (d), different scavengers like ammonium oxalate, benzoquinone, and isopropyl alcohol were used to demonstrate the reactive species. Here, the isopropyl alcohol scavenger exhibits lower degradation, proving that the OH radicals are active in the deterioration process. The degradation dropped from 87.74 to 46.65%. In order to remove organic contaminants from wastewater, these photocatalysts appear to be promising photocatalytic materials. It is explained by the strong interaction among the Fe and Co ions in cobalt ferrite material, demonstrating its excellent solution tolerance.

## 10 Conclusion

Sol-gel synthesized pure and GO-modified  $\text{CoFe}_2\text{O}_4$  nanoferrites display an inverse spinel structure with a relative increase in the crystallite size due to cationic rearrangement

and oxygen-embedded functional groups (C=OH, C=O, and COOH), respectively. Structural insights via DFT simulations also dictate a congruent analogy for dual compositions. However,  $O^{2-}$  coordination to binary interstices (tetrahedral and octahedral) constitutes an increased SSA for active charge transport with curtailed diffusion path length. Strong Co-Fe ionic bonding with Co-O-Fe superexchange interactions due to cationic distributions and low magnetic anisotropy invokes their ferrimagnetic response with pronounced saturation magnetization at low temperatures. A consequent rise in the crystallite size for GO-modified compositions relative to their host counterpart (27.78–40.25 nm) as reported experimentally illustrates a high impact on their optical response. An inverse reciprocity of crystallite size with the optical bandgap of spinel nanoferrites displays a competent photocatalytic activity of GO-modified nanocomposite with an increased surface area for charge adsorption. Thus, the ability to synthesize highly structured crystalline nanoferrites at commercial scales utilizing environmentally friendly processes is highly significant in waste-water treatment technologies.

**Supplementary Information** The online version contains supplementary material available at <https://doi.org/10.1007/s42247-024-00799-7>.

**Author contributions** Nandhini. G – Original draft, investigation, review & editing; Vignesh. D - Original draft, investigation, review & editing; Shobana. M. K. – conceptualization, review & editing, supervision; Pazhanivel. T - Formal analysis, investigation; Kavita. S - Formal analysis, investigation; Balaji. P – Formal analysis.

**Data availability** Data will be made available on the request.

## Declarations

**Conflict of interest** The authors declare that they have no known competing financial interests or personal relationships that could have appeared to influence the work reported in this paper.

## References

1. K. Parul, R. Kaur, P.P. Badru, S. Singh, Kaushal, Photodegradation of organic pollutants using heterojunctions: a review. *J. Environ. Chem. Eng.* **8**, 103666 (2020). <https://doi.org/10.1016/j.jece.2020.103666>
2. S.M. Peymani-Motlagh, N. Moeinian, M. Rostami, M. Fasihi-Ramandi, A. Sobhani-Nasab, M. Rahimi-Nasrabad, M. Eghbali-Arani, M.R. Ganjali, T. Jesionowski, H. Ehrlich, M.A. Karimi, N. Ajami, Effect of  $Gd^{3+}$ ,  $Pr^{3+}$  or  $Sm^{3+}$ -substituted cobalt-zinc ferrite on photodegradation of methyl orange and cytotoxicity tests. *J. Rare Earths.* **37**, 1288–1295 (2019). <https://doi.org/10.1016/j.jre.2019.04.010>
3. M.K. Shobana, H. Park, H. Choe, Effect of strontium substitution in cobalt ferrite: structural and optical studies. *Mater. Chem. Phys.* **272**, 124923 (2021). <https://doi.org/10.1016/j.matchemphys.2021.124923>
4. A. Azimi-fouladi, Falak, photocatalytic systems: a review. *J. Alloys Compd.* **961**, 171075 (2023). <https://doi.org/10.1016/j.jallcom.2023.171075>
5. S.A. Hassanzadeh-Tabrizi, H. Norbakhsh, R. Pournajaf, M. Tayebi, Synthesis of mesoporous cobalt ferrite/hydroxyapatite core-shell nanocomposite for magnetic hyperthermia and drug release applications. *Ceram. Int.* **47**, 18167–18176 (2021). <https://doi.org/10.1016/j.ceramint.2021.03.135>
6. F. Khan, M.S. Khan, S. Kamal, M. Arshad, S.I. Ahmad, S.A.A. Nami, Recent advances in graphene oxide and reduced graphene oxide based nanocomposites for the photodegradation of dyes. *J. Mater. Chem. C* **8**, 15940–15955 (2020). <https://doi.org/10.1039/d0tc03684f>
7. M. Sun, X. Han, S. Chen, Synthesis and photocatalytic activity of nano-cobalt ferrite catalyst for the photo-degradation various dyes under simulated sunlight irradiation. *Mater. Sci. Semicond. Process.* **91**, 367–376 (2019). <https://doi.org/10.1016/j.mssp.2018.12.005>
8. F. Jelokhani, S. Sheibani, A. Ataie, Adsorption and photocatalytic characteristics of cobalt ferrite-reduced graphene oxide and cobalt ferrite-carbon nanotube nanocomposites. *J. Photochem. Photobiol Chem.* **403**, 112867 (2020). <https://doi.org/10.1016/j.jphotochem.2020.112867>
9. A. Hassani, G. Çelikdağ, P. Eghbali, M. Sevim, S. Karaca, Ö. Metin, Heterogeneous sono-Fenton-like process using magnetic cobalt ferrite-reduced graphene oxide (CoFe<sub>2</sub>O<sub>4</sub>-rGO) nanocomposite for the removal of organic dyes from aqueous solution. *Ultrason. Sonochem.* **40**, 841–852 (2018). <https://doi.org/10.1016/j.ultsonch.2017.08.026>
10. M.A.M. Khan, W. Khan, M. Ahamed, J. Ahmed, M.A. Al-Gawati, A.N. Alhazaa, Silver-decorated Cobalt Ferrite nanoparticles anchored onto the Graphene sheets as Electrode materials for Electrochemical and Photocatalytic Applications. *ACS Omega.* **5**, 31076–31084 (2020). <https://doi.org/10.1021/acsomega.0c04191>
11. J. Chen, B. Yao, C. Li, G. Shi, An improved hummers method for eco-friendly synthesis of graphene oxide. *Carbon N Y.* **64**, 225–229 (2013). <https://doi.org/10.1016/j.carbon.2013.07.055>
12. M.K. Shobana, S. Sankar, V. Rajendran, Characterization of Co<sub>0.5</sub>Mn<sub>0.5</sub>Fe<sub>2</sub>O<sub>4</sub> nanoparticles. *Mater. Chem. Phys.* **113**, 10–13 (2009). <https://doi.org/10.1016/j.matchemphys.2008.07.083>
13. G. Nandhini, D. Vignesh, M.K. Shobana, S. Kavita, T. Pazhanivel, Experimental and DFT insights into optical and magnetic studies of graphene oxide/ZnFe<sub>2</sub>O<sub>4</sub> nanocomposites for enhanced photodegradation. *Appl. Nanosci.* **14**, 793–806 (2024). <https://doi.org/10.1007/s13204-024-03048-9>
14. S. Dudarev, G. Botton, Electron-energy-loss spectra and the structural stability of nickel oxide: an LSDA+U study. *Phys. Rev. B - Condens. Matter Mater. Phys.* **57**, 1505–1509 (1998). <https://doi.org/10.1103/PhysRevB.57.1505>
15. B. Kandasamy, S.B. Sussela, R. Sankararajan, P. Govindasamy, P. Thangavelu, V. Shanmugam, E. Nagaraj, V. Gopal, S. Manickam, R. Perumalsamy, Strontium-supported erbium oxide nanoparticles for efficient organic pollutant degradation under UV-Visible light. *J. Mater. Sci. Mater. Electron.* **33**, 20384–20398 (2022). <https://doi.org/10.1007/s10854-022-08855-w>
16. S. Di Mo, W. Ching, Electronic structure of normal, inverse, and partially inverse spinels in th system. *Phys. Rev. B - Condens. Matter Mater. Phys.* **54**, 16555–16561 (1996). <https://doi.org/10.1103/PhysRevB.54.16555>
17. H.L. Andersen, C. Granados-Mirallas, K.M.Ø. Jensen, M. Saura-Múzquiz, M. Christensen, The Chemistry of Spinel Ferrite nanoparticle nucleation, crystallization, and growth. *ACS Nano.* **18**, 9852–9870 (2024). <https://doi.org/10.1021/acsnano.3c08772>
18. S.B. Narang, K. Pubby, Nickel Spinel ferrites: a review. *J. Magn. Magn. Mater.* **519** (2021). <https://doi.org/10.1016/j.jmmm.2020.167163>

19. J.A. Flood-Garibay, M.A. Méndez-Rojas, Synthesis and characterization of magnetic wrinkled mesoporous silica nanocomposites containing Fe<sub>3</sub>O<sub>4</sub> or CoFe<sub>2</sub>O<sub>4</sub> nanoparticles for potential biomedical applications. *Colloids Surf. Physicochem Eng. Asp.* **615** (2021). <https://doi.org/10.1016/j.colsurfa.2021.126236>
20. Y. Fu, H. Chen, X. Sun, X. Wang, Combination of cobalt ferrite and graphene: high-performance and recyclable visible-light photocatalysis. *Appl. Catal. B Environ.* **111–112** (2012). <https://doi.org/10.1016/j.apcatb.2011.10.009>
21. V.H. Ojha, K.M. Kant, Investigation of structural and magnetic properties of strained CoFe<sub>2</sub>O<sub>4</sub> nanoparticles. *J. Phys. Chem. Solids.* **148**, 109655 (2021). <https://doi.org/10.1016/j.jpcs.2020.109655>
22. M.K. Shobana, G. Nandhini, S. Kavita, V. Suresh Kumar, T. Pazhanivel, Photocatalytic and magnetic properties of mg substituted cobalt ferrite. *Mater. Sci. Eng. B Solid-State Mater. Adv. Technol.* **286**, 116030 (2022). <https://doi.org/10.1016/j.mseb.2022.116030>
23. N. Hetache, Z. Charifi, T. Ghellab, H. Baaziz, F. Soyalp, Effect of octahedral cation on electronic, magnetic and optic properties of CoX<sub>2</sub>O<sub>4</sub> (X = cr, Mn and Fe) spinel compound. *Philos. Mag.* **102**, 166–188 (2022). <https://doi.org/10.1080/14786435.2021.1987546>
24. G. Wang, G. Chen, Z. Wei, X. Dong, M. Qi, Multifunctional Fe<sub>3</sub>O<sub>4</sub>/graphene oxide nanocomposites for magnetic resonance imaging and drug delivery. *Mater. Chem. Phys.* **141**, 997–1004 (2013). <https://doi.org/10.1016/j.matchemphys.2013.06.054>
25. G. Wang, Y. Ma, X. Dong, Y. Tong, L. Zhang, J. Mu, Y. Bai, J. Hou, H. Che, X. Zhang, Facile synthesis and magnetorheological properties of superparamagnetic CoFe<sub>2</sub>O<sub>4</sub>/GO nanocomposites. *Appl. Surf. Sci.* **357**, 2131–2135 (2015). <https://doi.org/10.1016/j.apsusc.2015.09.196>
26. F. Sharifianjazi, M. Moradi, N. Parvin, A. Nemati, A. Jafari Rad, N. Sheysi, A. Abouchenari, A. Mohammadi, S. Karbasi, Z. Ahmadi, A. Esmaeilkhani, M. Irani, A. Pakseresht, S. Sahmani, Shahedi Asl, magnetic CoFe<sub>2</sub>O<sub>4</sub> nanoparticles doped with metal ions: a review. *Ceram. Int.* **46**, 18391–18412 (2020). <https://doi.org/10.1016/j.ceramint.2020.04.202>
27. V.P. Senthil, J. Gajendiran, S.G. Raj, T. Shanmugavel, G. Ramesh Kumar, C. Parthasaradhi, Reddy, Study of structural and magnetic properties of cobalt ferrite (CoFe<sub>2</sub>O<sub>4</sub>) nanostructures. *Chem. Phys. Lett.* **695**, 19–23 (2018). <https://doi.org/10.1016/j.cplett.2018.01.057>
28. A.V. Ravindra, M. Chandrika, C. Rajesh, P. Kollu, S. Ju, S.D. Ramarao, Simple synthesis, structural and optical properties of cobalt ferrite nanoparticles. *Eur. Phys. J. Plus.* **134** (2019). <https://doi.org/10.1140/epjp/i2019-12690-2>
29. G. Wang, Y. Ma, Z. Wei, M. Qi, Development of multifunctional cobalt ferrite/graphene oxide nanocomposites for magnetic resonance imaging and controlled drug delivery. *Chem. Eng. J.* **289**, 150–160 (2016). <https://doi.org/10.1016/j.cej.2015.12.072>
30. P.R. Jubu, O.S. Obaseki, A. Nathan-Abutu, F.K. Yam, Y. Yusof, M.B. Ochang, Dispensability of the conventional Tauc's plot for accurate bandgap determination from UV–vis optical diffuse reflectance data. *Results Opt.* **9**, 100273 (2022). <https://doi.org/10.1016/j.rio.2022.100273>
31. A. Murali, P.K. Sarswat, M.L. Free, Minimizing electron-hole pair recombination through band-gap engineering in novel ZnO-CeO<sub>2</sub>-rGO ternary nanocomposite for photoelectrochemical and photocatalytic applications. *Environ. Sci. Pollut. Res.* **27**, 25042–25056 (2020). <https://doi.org/10.1007/s11356-020-08990-z>
32. Y.S. Vidya, H.C. Manjunatha, K.N. Sridhar, Comparative study of multi functional nanoferrites for radiation shielding, photoluminescence and antibacterial properties. *Inorg. Chem. Commun.* **138**, 109217 (2022). <https://doi.org/10.1016/j.inoche.2022.109217>
33. S. Agrawal, A. Parveen, A. Azam, Structural, electrical, and optomagnetic tweaking of Zn doped CoFe<sub>2-x</sub>ZnxO<sub>4-δ</sub> nanoparticles. *J. Magn. Mater.* **414**, 144–152 (2016). <https://doi.org/10.1016/j.jmmm.2016.04.059>
34. K.F. Lin, H.M. Cheng, H.C. Hsu, L.J. Lin, W.F. Hsieh, Band gap variation of size-controlled ZnO quantum dots synthesized by sol-gel method. *Chem. Phys. Lett.* **409**, 208–211 (2005). <https://doi.org/10.1016/j.cplett.2005.05.027>
35. S. Jauhar, J. Singh, K. Chandra, S. Bansal, S. Singhal, Structural, morphological, magnetic and optical properties of chromium substituted strontium ferrites, SrCr<sub>x</sub>Fe<sub>12-x</sub>O<sub>19</sub> (x = 0.5, 1.0, 1.5, 2.0 and 2.5) annealed with potassium halides. *Powder Technol.* **212**, 193–197 (2011). <https://doi.org/10.1016/j.powtec.2011.05.014>
36. K.L. Routray, S. Saha, D. Behera, Effect of CNTs blending on the structural, dielectric and magnetic properties of nanosized cobalt ferrite. *Mater. Sci. Eng. B Solid-State Mater. Adv. Technol.* **226**, 199–205 (2017). <https://doi.org/10.1016/j.mseb.2017.09.021>
37. E. Jha, A. Akbari-fakhrabadi, D.K. Ray, V.S. Benitha, K. Jeyasubramanyan, Memorial University of Newfoundland, Department of Physics and Physical Oceanography, (2019)
38. Y. Ding, Q. Liao, S. Liu, H. Guo, Y. Sun, G. Zhang, Y. Zhang, Reduced Graphene Oxide Functionalized with Cobalt Ferrite Nanocomposites for enhanced efficient and Lightweight Electromagnetic Wave absorption. *Sci. Rep.* **6**, 1–9 (2016). <https://doi.org/10.1038/srep32381>
39. O. Dehghani Dastjerdi, H. Shokrollahi, S. Mirshekari, A review of synthesis, characterization, and magnetic properties of soft spinel ferrites. *Inorg. Chem. Commun.* **153**, 110797 (2023). <https://doi.org/10.1016/j.inoche.2023.110797>
40. B.R. Guduri, A.S. Luyt, Structure and mechanical properties of polycarbonate modified clay nanocomposites. *J. Nanosci. Nanotechnol.* **8**, 1880–1885 (2008). <https://doi.org/10.1166/jnn.2008.017>
41. Q. Miao, L. Wang, Z. Liu, B. Wei, F. Xu, W. Fei, Magnetic properties of N-doped graphene with high Curie temperature. *Sci. Rep.* **6**, 1–10 (2016). <https://doi.org/10.1038/srep21832>
42. C. Aziz, B. Azhdar, Synthesis of dysprosium doped cobalt ferrites nanoparticles by solgel auto-combustion method and influence of grinding techniques on structural, morphological, and magnetic properties. *J. Magn. Mater.* **542**, 168577 (2022). <https://doi.org/10.1016/j.jmmm.2021.168577>
43. T. Dippong, E.A. Levei, O. Cadar, Formation, structure and magnetic properties of mfe<sub>2</sub>o<sub>4</sub>@sio<sub>2</sub> (M = co, mn, zn, Ni, Cu) nanocomposites, materials (Basel). **14** (2021) 1–15. <https://doi.org/10.3390/ma14051139>
44. F.G. da Silva, J. Depeyrot, A.F.C. Campos, R. Aquino, D. Fiorani, D. Peddis, Structural and Magnetic Properties of Spinel Ferrite Nanoparticles. *J. Nanosci. Nanotechnol.* **19**, 4888–4902 (2019). <https://doi.org/10.1166/jnn.2019.16877>
45. A.M. Davarpanah, A.A. Mirzae, M. Sargazi, M. Feizi, Magnetic properties of Fe-Ni nanoparticles prepared by co-precipitation method. *J. Phys. Conf. Ser.* **126**, 1–11 (2008). <https://doi.org/10.1088/1742-6596/126/1/012065>
46. N. Abinaya, M.C. Robert, N. Srinivasan, S. Saravanakumar, Electron density mapping and bonding in Mn doped CoFe<sub>2</sub>O<sub>4</sub> using XRD, and its correlation with room temperature optical and magnetic properties. *J. Magn. Mater.* **580**, 170938 (2023). <https://doi.org/10.1016/j.jmmm.2023.170938>
47. A. Chakrabarti, S. Sarkar, S.M. Banerjee, A. Bandyopadhyay, S. Chattopadhyay, Materials Today: Proceedings Investigating the modification in structural properties of cobalt ferrite nanoparticles with increasing annealing temperature, *Mater. Today Proc.* (2023). <https://doi.org/10.1016/j.matpr.2023.05.006>
48. S. Sarmah, K.P. Patra, P.K. Maji, S. Ravi, T. Bora, A comparative study on the structural, magnetic and dielectric properties of

- magnesium substituted cobalt ferrites. *Ceram. Int.* **49**, 1444–1463 (2023). <https://doi.org/10.1016/j.ceramint.2022.09.126>
49. S. Menchaca-Nal, J.A. Jativa-Herrera, O. Moscoso-Londoño, L.G. Pampillo, R. Martínez-García, M. Knobel, C.L. Londoño-Calderón, Composite magnetic properties of cobalt ferrite nanoparticles embedded in bacterial nanocellulose of different porosity levels. *Mater. Chem. Phys.* **303** (2023). <https://doi.org/10.1016/j.matchemphys.2023.127798>
50. Y. Lu, M. Yousaf, M.N. Akhtar, A. Noor, M. Akbar, M.A.K.Y. Shah, S. Yan, F. Wang, Effect of Gd and Co contents on the microstructural, magneto-optical and electrical characteristics of cobalt ferrite (CoFe<sub>2</sub>O<sub>4</sub>) nanoparticles. *Ceram. Int.* **48**, 2782–2792 (2022). <https://doi.org/10.1016/j.ceramint.2021.10.067>
51. P. Sowjanya, N.P. Kumar, A. Chelvane, M.V.R. Reddy, Synthesis and analysis of low field high magnetostrictive Ni-Co ferrite for magneto-electric energy harvesting applications. *Mater. Sci. Eng. B Solid-State Mater. Adv. Technol.* **279** (2022). <https://doi.org/10.1016/j.mseb.2022.115674>
52. F.R. Mariosi, J. Venturini, A. da Cas Viegas, C.P. Bergmann, Lanthanum-doped spinel cobalt ferrite (CoFe<sub>2</sub>O<sub>4</sub>) nanoparticles for environmental applications. *Ceram. Int.* **46**, 2772–2779 (2020). <https://doi.org/10.1016/j.ceramint.2019.09.266>
53. S. Amiri, H. Shokrollahi, Magnetic and structural properties of RE doped co-ferrite (RE = nd, Eu, and Gd) nano-particles synthesized by co-precipitation. *J. Magn. Magn. Mater.* **345**, 18–23 (2013). <https://doi.org/10.1016/j.jmmm.2013.05.030>
54. A. Ditta, M.A. Khan, M. Junaid, R.M.A. Khalil, M.F. Warsi, Structural, magnetic and spectral properties of Gd and Dy co-doped dielectrically modified co-ni (Ni<sub>0.4</sub>Co<sub>0.6</sub>Fe<sub>2</sub>O<sub>4</sub>) ferrites. *Phys. B Condens. Matter.* **507**, 27–34 (2017). <https://doi.org/10.1016/j.physb.2016.11.030>
55. X. Wang, M. Zhu, L.K. Koopal, W. Li, W. Xu, F. Liu, J. Zhang, Q. Liu, X. Feng, D.L. Sparks, Effects of crystallite size on the structure and magnetism of ferrihydrite. *Environ. Sci. Nano.* **3**, 190–202 (2016). <https://doi.org/10.1039/c5en00191a>
56. A.H. Navidpour, S. Abbasi, D. Li, A. Mojiri, J.L. Zhou, Investigation of advanced oxidation process in the Presence of TiO<sub>2</sub> Semiconductor as Photocatalyst: property, Principle, Kinetic Analysis, and photocatalytic activity. *Catalysts.* **13** (2023). <https://doi.org/10.3390/catal13020232>
57. M. Fu, Q. Jiao, Y. Zhao, In situ fabrication and characterization of cobalt ferrite nanorods/graphene composites. *Mater. Charact.* **86**, 303–315 (2013). <https://doi.org/10.1016/j.matchar.2013.10.019>
58. E. Elanthamilan, I.B. Elizabeth, S.F. Wang, I.S. Lydia, Strontium hexaferrite microspheres: synthesis, characterization and visible-light-driven photocatalytic activity towards the degradation of methylene blue dye. *Opt. Mater. (Amst.)* **137**, 113565 (2023). <https://doi.org/10.1016/j.optmat.2023.113565>

**Publisher's Note** Springer Nature remains neutral with regard to jurisdictional claims in published maps and institutional affiliations.

Springer Nature or its licensor (e.g. a society or other partner) holds exclusive rights to this article under a publishing agreement with the author(s) or other rightsholder(s); author self-archiving of the accepted manuscript version of this article is solely governed by the terms of such publishing agreement and applicable law.